

VAE-GANs for Probabilistic Compressive Image Recovery: Uncertainty Analysis

Vineet Edupuganti¹ Morteza Mardani¹ Joseph Cheng^{1,2} Shreyas Vasanawala² John Pauly¹

Abstract

Recovering high-quality images from limited sensory data is a challenging computer vision problem that has received significant attention in recent years. In particular, solutions based on deep learning, ranging from autoencoders to generative models, have been especially effective. However, comparatively little work has centered on the robustness of such reconstructions in terms of the generation of realistic image artifacts (known as hallucinations) and quantifying uncertainty. In this work, we develop experimental methods to address these concerns, utilizing a variational autoencoder-based generative adversarial network (VAE-GAN) as a probabilistic image recovery algorithm. We evaluate the model’s output distribution statistically by exploring the variance, bias, and error associated with generated reconstructions. Furthermore, we perform eigen analysis by examining the Jacobians of outputs with respect to the aliased inputs to more accurately determine which input components can be responsible for deteriorated output quality. Experiments were carried out using a dataset of Knee MRI images, and our results indicate factors such as sampling rate, acquisition model, and loss function impact the model’s robustness. We also conclude that a wise choice of hyperparameters can lead to the robust recovery of MRI images.

1. Introduction

Solving linear inverse problems is one of the primary challenges in many image recovery tasks, encompassing both the natural and medical domains. This recovery process is made especially difficult by the fact that inputs are oftentimes plagued by insufficient data. While iterative algo-

rithms based on compressed sensing (CS) can oftentimes produce reasonable reconstructions, they are highly inefficient. As such, the last several years have witnessed an explosion of deep learning (DL) based approaches such as generative adversarial networks (GANs) and convolutional autoencoders (CAEs) that offer orders of magnitude speed-up while simultaneously improving accuracy (Radford et al., 2015; Quan et al., 2017; Zhu et al., 2018; Lee et al., 2017; Bora et al., 2017; Mousavi et al., 2015).

One major shortcoming of these studies, however, is a relative lack of focus on the robustness of DL architectures in inverse problems. Not only is the introduction of image artifacts fairly common using such models, but there do not currently exist suitable empirical methods that enable the quantification of uncertainty (Mardani et al., 2018). Such methods, however, could have incredible utility both as an evaluation metric and as a way of gaining interpretability regarding risk factors for a given model and dataset (Kendall & Gal, 2017).

Contributions. To this end, this work introduces experimental procedures that can provide insight into the robustness of a specific DL scheme. In doing so, we develop a VAE-GAN model for image recovery, which is notable for its high performance and probabilistic nature which inherently facilitates the analysis of model uncertainty. We first use standard statistical methods to better understand the variations and errors in the output image distribution under different hyperparameter settings (Harrell et al., 1996). We then proceed to the eigen analysis of the DL model, whereby we explore gradients of the outputs with respect to the inputs and the corresponding singular value magnitudes over the course of training. This approach elucidates the extent to which adversarial perturbations to specific regions of the input can have influence and serves as a promising way of localizing uncertainty.

2. Preliminaries and Problem Statement

To evaluate the VAE-GAN model and our proposed methods, we use a dataset of medical images, which have become increasingly important with the growing prevalence of various imaging modalities. Magnetic Resonance Imaging (MRI),

¹Department of Electrical Engineering, Stanford University, Stanford, California, USA ²Department of Radiology, Stanford University, Stanford, California, USA. Correspondence to: Vineet Edupuganti <ve5@stanford.edu>.

specifically, has become a critical healthcare tool over the years due to its unique ability to non-invasively obtain information about tissue composition, structure, and anatomy. As a result, the development of accurate and rapid MRI reconstruction methods could represent a major step forward for the field of medical imaging, with the potential to enable powerful applications like diagnostic-guided surgery or cost-effective pediatric scanning without anesthesia (Hynnen et al., 1993; Vasanawala & Lustig, 2011). However, to achieve a high spatiotemporal resolution, significant undersampling is typically employed, leading to ill-posed inverse problems.

Specifically, given an observation y , we need to recover an image x , where $y = \Phi x$ (with Φ consisting of a Fourier transform operator followed by subsampling), $y \in \mathbb{C}^m$, $x \in \mathbb{C}^n$, and $m \ll n$, necessitating the use of prior information (Lustig et al., 2007).

DL-based MRI reconstruction has several advantages, such as being incredibly rapid and reasonably accurate (Greenspan et al., 2016). One theoretical risk with such DL-based reconstruction methods, however, is the introduction of realistic artifacts, or so-termed "hallucinations", which can prove costly in a domain as sensitive as medical imaging by misleading radiologists and resulting in incorrect diagnoses (Xu et al., 2014; Yang et al., 2018). Hence, a motivation of this work is to examine the extent and underlying source of these hallucinations and, in so doing, analyze the robustness of DL techniques in MRI reconstruction problems.

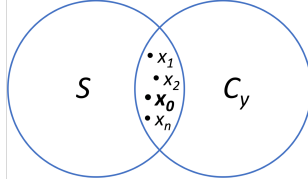


Figure 1. Set of admissible solutions, where x_0 represents the true image.

Problem statement. More concretely, it stands to reason that there could exist multiple recovered images that look both realistic and feasible given a specific data acquisition process, and that one of these might represent hallucination. Thus, the objective of this work is to model the intersection between a clean image manifold \mathcal{S} learned by a VAE-GAN and a data consistent subspace $\mathcal{C}_y := \{x \in \mathbb{C}^n : y = \Phi x\}$, since we could find hallucinated images x_1, x_2 , or x_n , in addition to the true image x_0 (see Fig. 1).

3. Uncertainty Analysis

The VAE served as the generator function of the GAN, while the discriminator was a CNN. At test time, latent code vectors were sampled from a normal distribution $z \sim \mathcal{N}(0, 1)$

to generate new reconstructions that were evaluated for hallucinations. Data consistency was applied to all network outputs, which we found essential to obtaining high SNR. Figure 2 depicts the various components of the model.

The data consistent subspace was obtained by applying an affine projection based on the undersampling mask to ensure that reconstructions did not deviate from physical measurement (Mardani et al., 2018). The VAE, in turn, was particularly useful to use as a generator function because it learns a probability distribution of realistic images that facilitates the exploration process of the manifold \mathcal{S} . By randomly sampling latent code vectors corresponding to specific images, then, we were able to traverse the space comprising $\mathcal{S} \cap \mathcal{C}_y$ and evaluate the results visually and statistically to determine whether or not hallucinations could be generated.

$$\min_{\Theta_d} \mathbb{E}_x [(1 - \mathcal{D}(x; \Theta_d))^2] + \mathbb{E}_y [(\mathcal{D}(x_{\text{out}}; \Theta_d))^2] \quad (1)$$

$$\begin{aligned} \min_{\Theta_g} \mathbb{E}_{x,y} (1 - \lambda) [\|x - x_{\text{out}}\|_2 + \eta D_{KL}(\mathcal{N}(\mu, \sigma) \| \mathcal{N}(0, 1))] \\ + \lambda \mathbb{E}_y [(1 - \mathcal{D}(x_{\text{out}}; \Theta_d))^2] \end{aligned} \quad (2)$$

The loss functions used in training were based on the mixture of pixel-wise ℓ_2 and the adversarial GAN loss. The discriminator (\mathcal{D}) loss (shown in 1) was designed to have ground truth images receive a label of 1 and generator outputs (the fake images) receive a label of 0, in order to correctly distinguish between real slices and their corresponding reconstructions. The generator loss function (as in 2) was comprised of two parts. The first was a weighted sum of pixel-wise MSE for the output and a KL-divergence term for the latent code (based on μ, σ for a given batch) to ensure the model was penalized for having outputs dissimilar to the fully-sampled images or latent spaces that failed to follow a normal distribution (Dosovitskiy & Brox, 2016; Kingma & Welling, 2013). The second was a term to encourage the generator to "fool" the discriminator (have \mathcal{D} output a 1 for the reconstructed image). The parameters η and λ were responsible for controlling the weights of the KL-divergence term and the discriminator feedback term, respectively. As η increased, the integrity of the generator latent code was preserved at the expense of reconstruction quality, which was dictated by the MSE term. Likewise, as λ increased the influence of the discriminator became larger, enhancing the modeling of realistic image components, but leading to higher MSE values overall. In most experiments, loss converged over approximately 20K iterations, and final results showed minimal differences between the reconstructed images and the fully-sampled ground-truth, as measured by both MSE and SNR.

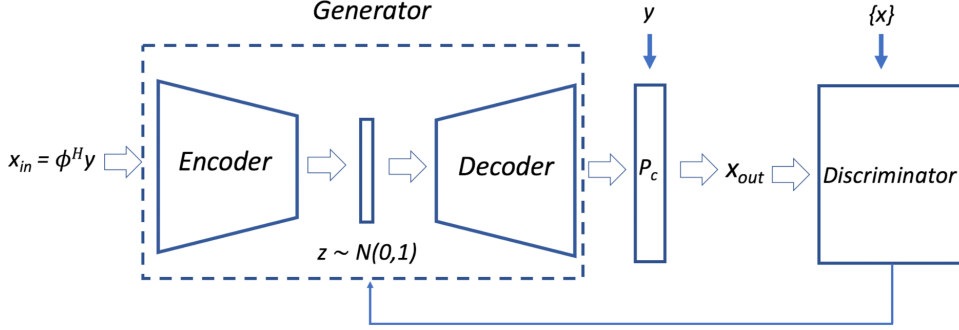


Figure 2. The model architecture, with aliased input images feeding into the VAE encoder, the latent code feeding into the VAE decoder, and data consistency applied to obtain the output reconstruction. This output serves as an input to the GAN discriminator, which in turn sends feedback to the generator.

4. Evaluations

4.1. Dataset

The Knee dataset utilized in training and testing was obtained from 19 patients with a 3T GE MR750 scanner ([mri](#)). Each volume consisted of 320 2D slices of dimension 320×256 that were divided into training, validation, and test examples, and a 5-fold variable density undersampling mask with radial view ordering (designed to preserve low-frequency structural elements) was used to produce aliased input images x_{in} for the model to reconstruct ([Cheng et al., 2013](#)).

4.2. Network architecture

The VAE encoder was composed of 4 layers formed through a sequence of strided convolution operations followed by ReLU activations and batch normalization ([van den Oord et al., 2017](#)). Latent space mean, μ , and standard deviation, σ , were represented by fully connected layers. The VAE decoder also had 4 layers and utilized transpose convolution operations for upsampling ([Jégou et al., 2017](#)). Skip connections were utilized to improve gradient flow through the network, thereby reserving randomness primarily for high-frequencies, which is appropriate given that low-frequencies are preserved in the measurements anyway ([Dieng et al., 2018; Pezeshki et al., 2016](#)). The discriminator function of the GAN was an 8-layer CNN.

4.3. Training behavior

Training was completed over the course of 30K iterations under an array of different conditions. We utilized the Adam SGD optimizer with a mini-batch size of 4, an initial learning rate of 5×10^{-5} that was halved every 5K iterations, and a momentum parameter of 0.9. Models and experiments were developed using TensorFlow on an NVIDIA Titan X Pascal GPU with 12GB RAM. A version of our TensorFlow

source code is publicly available via Github ([git](#)).

The discriminator real loss, the discriminator fake loss, and the generator ℓ_2 loss are shown in Fig. 3 for the standard case with 5-fold undersampling and pure MSE loss (row 1) in addition to the case with GAN loss $\lambda = 0.10$ (row 2) and the case with two model iterations (models are stacked together with shared parameters, results are shown in row 3). In all cases, loss decreases and converges after approximately 20K iterations. The ℓ_2 loss tends to be noisier than the discriminator losses. It is possible that further tuning of hyperparameters such as the learning rate and decay could help limit some of these fluctuations.

The ℓ_2 loss with GAN (row 2, column 3 in Fig. 3) provides a useful look at the details of the training process. The model is trained with MSE loss only for the first 1K iterations before transitioning to GAN loss. Thus, the loss decreases during the MSE phase before immediately increasing in correspondence with the start of the GAN phase. Loss eventually decreases to its initial value and stabilizes, but the convergence occurs at a much higher value than the baseline case in row 1. This behavior is expected since GAN reconstructions yield lower SNR and higher MSE loss, in exchange for sharper images and more accurate modeling of high-frequency image components.

Row 3 of Fig. 3 demonstrates that the discriminator losses are more noisy with two model iterations than in the other cases, although convergence occurs fairly quickly. This trend could be due to the more challenging training process associated with the stacked model. However, as expected with a deeper model, the ℓ_2 loss is lower with two model iterations than just one. Additional fine-tuning of hyperparameters and the model architecture would likely provide marginal loss improvements in all cases.

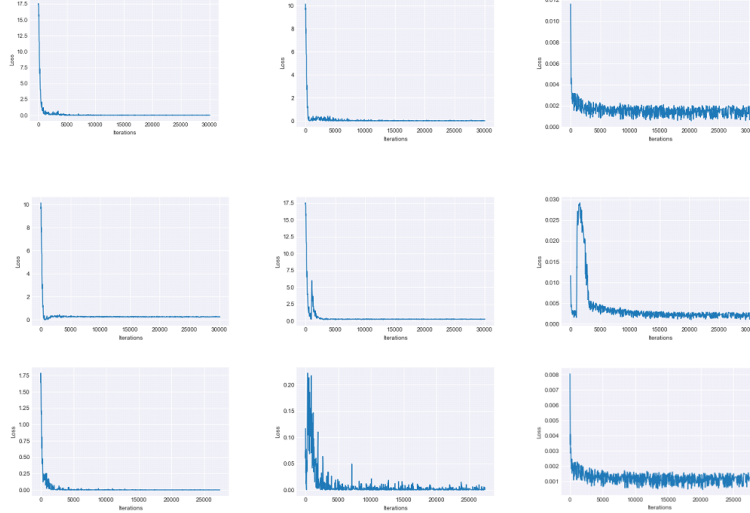


Figure 3. Discriminator real loss, discriminator fake loss, and generator ℓ_2 loss under various conditions. Row 1: 5-fold undersampling and no GAN loss. Row 2: 5-fold undersampling with 10 percent GAN loss. Row 3: 5-fold undersampling with no GAN loss and two model iterations

4.4. Individual reconstructions

Figure 4 shows sample model reconstructions for representative test slices with different hyperparameters. As the number of iterations increases from one to two (columns 2 and 3 versus 4 and 5), the resulting outputs improve in quality (corresponding to a roughly 1 dB gain in SNR). Figure 5 shows how progressively increasing values of GAN loss (from columns 2 through 6) introduce high-frequency components and lead to sharper outputs. Nevertheless, as the GAN loss weight exceeds 10 percent, the image quality deteriorates drastically, leading to very poor quality reconstructions. Furthermore, it is easy to see the greatly increased presence of artifacts with higher GAN loss, indicating potential concerns with robustness. However, once GAN loss rises to 25 percent, these artifacts are so clearly unrealistic that they represent inadequate image recovery rather than true hallucinations.

4.5. Variance, bias, and error

After training was completed, 1K outputs corresponding to different reference slices were generated by feeding a test image into the model and sampling from the resulting output distribution. To provide a better sense of the hallucination risks that can be attributed to the VAE-GAN architecture, we show the mean of the 1K reconstructed outputs for a representative slice and plot the pixel-wise variance, bias (using the mean image as the prediction), and error (Fig. 6), utilizing the common relation $\text{error} = \text{bias}^2 + \text{variance}$ (Tibshirani, 1996). The concept of bias and variance is important in the analysis of hallucinations and uncertainty because both the difference from the mean and the inherent

variability across realizations provide information on the portions of a given image most susceptible to the introduction of realistic artifacts (along with precise numbers that can be used for comparison with different hyperparameter and model schemes). Furthermore, the pixel maps allow for a greater understanding of the spatial correlations between bias and variance, as well as inter-pixel dependencies.

The results in Fig. 6 indicate that variance, bias, and error all increase as the undersampling rate increases (rows 1 and 3) and the GAN loss weight increases (rows 2 through 4). This indicates that high-frequency components of the image, which GANs are particularly adept at modeling and which highly undersampled images do not retain, pose the greatest risk in terms of hallucination. Nevertheless, with a reasonably conservative undersampling rate and choice of GAN weight λ , the likelihood of major hallucinations occurring is quite low.

4.6. Eigen analysis

While the variability induced by the model is an extremely valuable consideration when looking at hallucinations and uncertainty, the input data itself can also play a fairly significant role in the generation or omission of realistic artifacts (Tygert et al., 2018). For that reason, we explore the gradients of the output reconstructions with respect to the aliased input images themselves (i.e. the Jacobian), $\mathcal{J} := \frac{\partial x_{out}}{\partial x_{in}}$, noting that the model weights are also used in the computation (Henaff et al., 2015). The resulting map provides an indication of the extent to which each input pixel influences the output image. Figure 7 shows this gradient map (in the frequency domain) as well as the corresponding singular

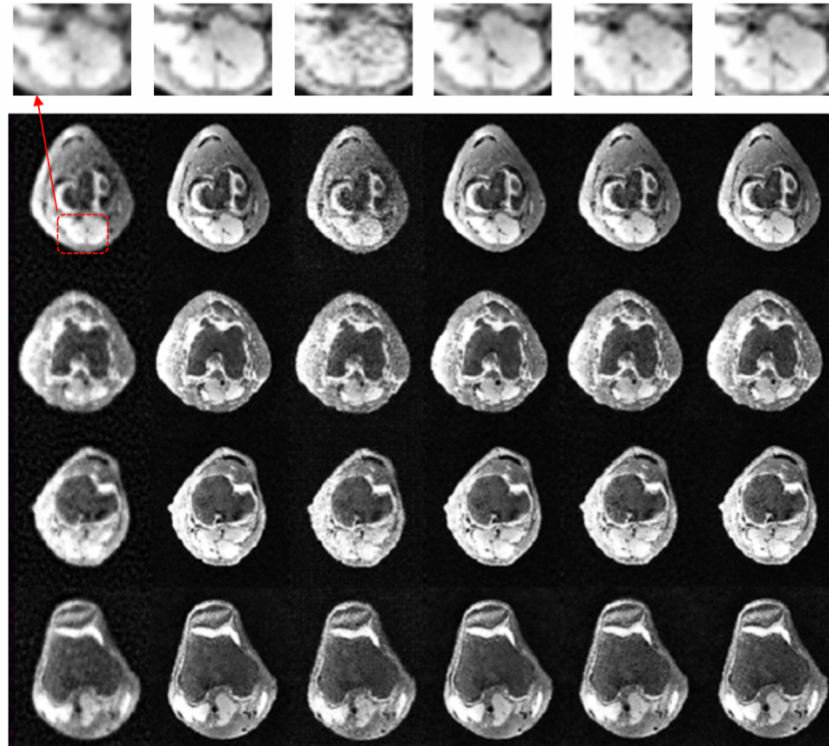


Figure 4. The aliased input, reconstructions with one model iteration and pure MSE loss, one iteration and 10 percent GAN loss, two model iterations and pure MSE loss, and two iterations and 10 percent GAN loss, and the ground truth for four representative slices.

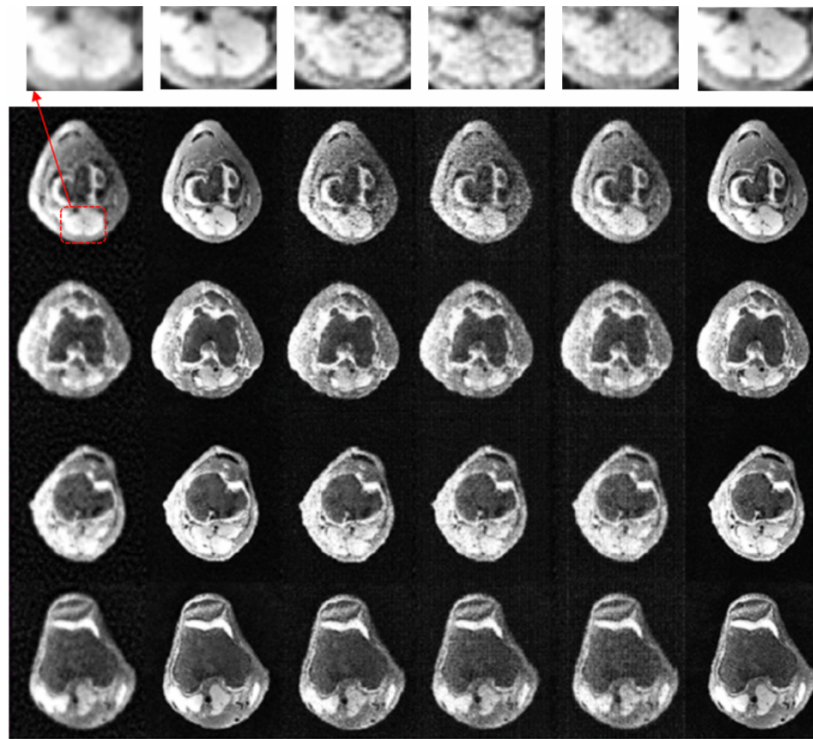


Figure 5. The aliased input, model (one iteration) reconstructions with pure MSE loss, 10 percent GAN loss, 25 percent GAN loss, and 50 percent GAN loss, and the ground truth for four representative slices.

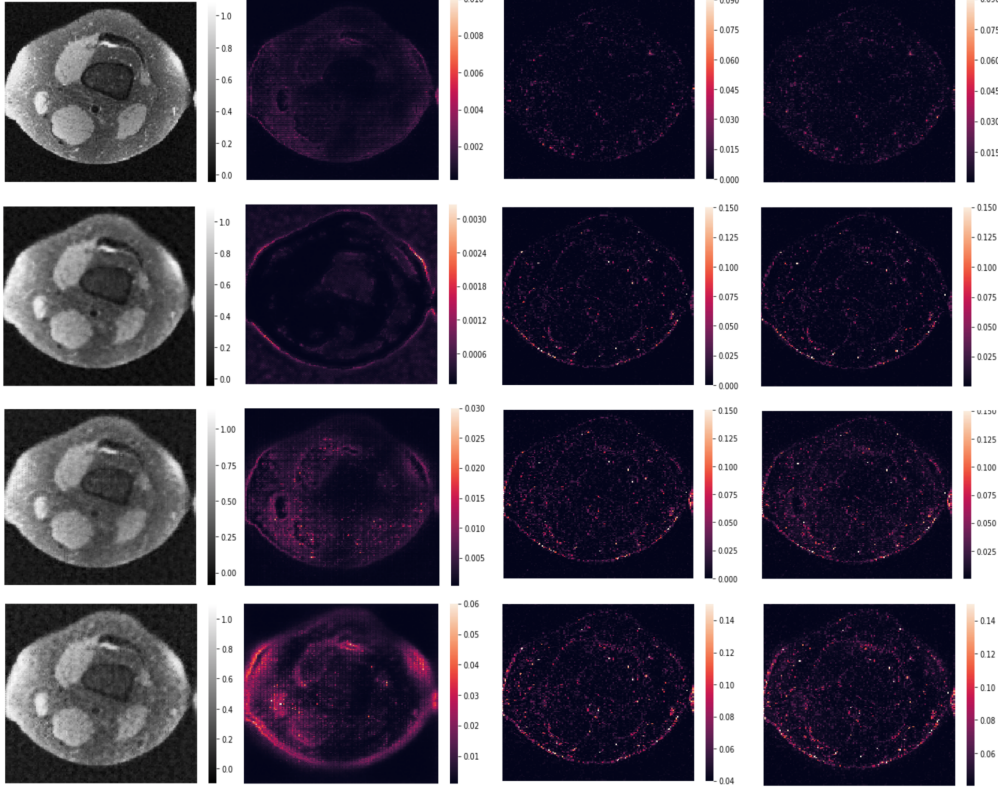


Figure 6. Mean reconstruction, pixel-wise variance, bias, and error for a given reference slice across all realizations. Row 1: 5 percent GAN loss ($\lambda = 0.05$) with 2-fold undersampling. Row 2: 0 percent GAN loss ($\lambda = 0$) with 5-fold undersampling. Row 3: 5 percent GAN loss ($\lambda = 0.05$) with 5-fold undersampling. Row 4: 10 percent GAN loss ($\lambda = 0.10$) with 5-fold undersampling.

values $\{\sigma_i(\mathcal{J})\}$ (represented as a diagonal matrix) over the course of 20K iterations of model training (rows 1 and 2) and for different slices after the model training (rows 3 and 4) for the case of 5-fold undersampling with no GAN loss.

The first row of Fig. 7 indicates that as training progresses low-frequency components of the input are de-emphasized in favor of high-frequency ones. Additionally, over time the pixels corresponding to the bright vertical line in the center of the frequency domain gain more influence, suggesting one possible explanation for how certain hallucinations can be learned by the model. Furthermore, during the training process the singular values of the gradient, shown in the second row, become more concentrated, meaning that there are a few large singular values with the rest being very small. This trend likely indicates that the model learns to prioritize certain small portions of the input image.

The third row of Fig. 7 shows that as the test image varies, the gradient of the output with respect to the input for the trained model varies primarily in the low frequencies which are responsible for structure, with the vertical streak present in all cases. The fourth row shows that the singular values

of the different images evolve similarly, with only a few large values in all cases.

Similar to the statistical evaluations, it is possible to derive precise values for the influence of regions in the aliased images from the gradient maps, which enables differentiation of models and settings on the basis of resistance to adversarial inputs (a proxy for uncertainty). Indeed, by understanding the end-to-end transfer function of the system, we are able to obtain a better sense of the frequencies most responsible for hallucination. Based on the results above, it seems that high-frequency components of the input in addition to model parameters are the likeliest cause of increased hallucination risk, which corroborates the variance, bias, and error results.

4.7. Closer comparison of singular values

4.7.1. EVOLUTION

Figure 8 provides a more detailed glimpse of how the magnitudes of the singular values of the gradient with respect to the input evolve over the course of training under specific

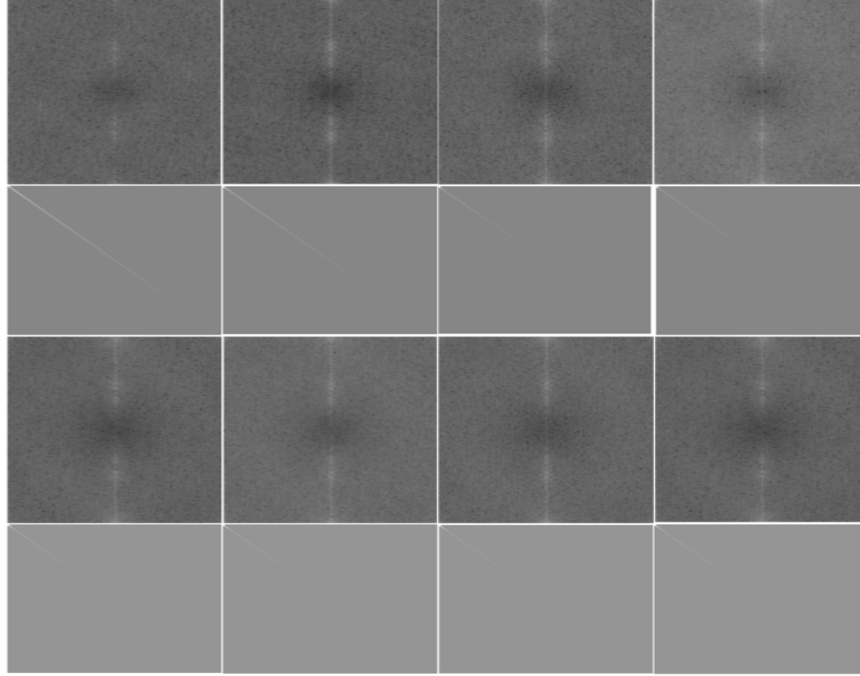


Figure 7. Row 1: FFT of the gradient of the output with respect to the input after 1K, 5K, 10K, and 20K iterations of training. Row 2: Singular values of the gradient of the output with respect to the input after 1K, 5K, 10K, and 20K iterations of training. Row 3: FFT of the gradient of the output with respect to the input for four different test images with the fully trained model. Row 4: Singular values of the gradient of the output with respect to the input for four different test images with the trained model.

conditions. In the first column, we see that there is very similar behavior between one model iteration and two model iterations with pure MSE loss. However, the magnitudes of the singular values with one model iteration are about twice that of two model iterations. Hence, it is possible that input data has more influence with a smaller number of iterations because the model has comparatively less representational capacity. Counterintuitively, adding in 10 percent GAN loss to these cases (as in the second column) results in significantly smaller singular value magnitudes as well. However, as noted in the earlier sections, the singular values are much less concentrated (i.e. the difference between the maximum and the median is smaller). Such results suggest that training with high GAN loss makes the model more susceptible to hallucinations, given that more regions in the input have substantial (albeit smaller) impact (Moosavi-Dezfooli et al., 2017).

4.7.2. DECAY

It is also useful to see the spread of the singular values by viewing the sorted magnitudes at a given iteration of training, as shown in Fig. 9, which shows the results for pure MSE loss (baseline) and 10 percent GAN weight with one iteration and two iterations after 1, 15K, and 30K iterations of training (the one model iteration curves overlap

in the first plot as do the two iteration ones). With pure MSE loss in both the one model iteration and two model iteration cases, we observe that the magnitudes associated with the largest singular values increase between 1 and 15K iterations before stabilizing. Meanwhile, the magnitudes associated with the smallest singular values decreases. On the other hand, in the GAN cases, the reverse holds true: the largest singular values decrease in magnitude and the smallest ones increase by a small amount. After the 30K iterations of training, the decay rate of the singular values is lowest for the case with GAN loss and one model iteration, followed by the baseline with one model iteration, GAN loss with two model iterations, and finally the baseline with two model iterations. Thus, both increased GAN loss and decreased model iterations lead to less concentrated and more equal singular values. On the positive side, this longer tail in the singular value distribution associated with high GAN loss and fewer iterations indicates that the learned model does not overemphasize low-frequencies and also values high-frequency modes. However, as stated above, this effect could have direct implications on decreased robustness, since there is less immunity to perturbations for more regions in the input (Papernot et al., 2016).

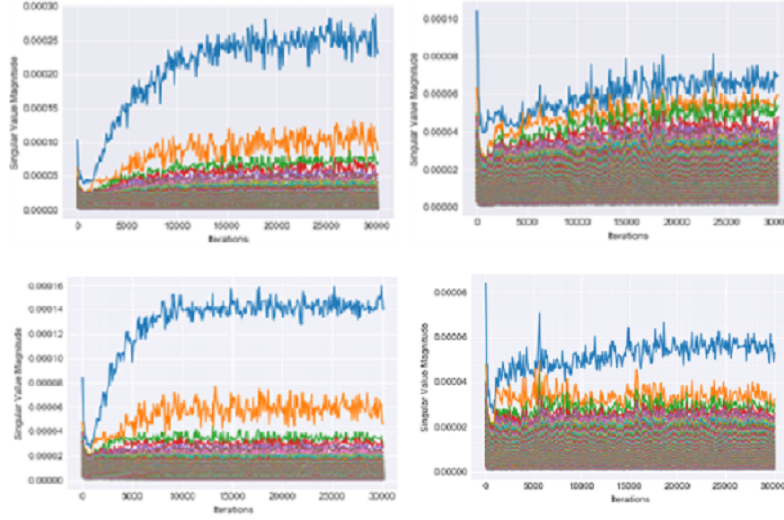


Figure 8. Singular value magnitudes over 30,000 iterations of training with pure MSE loss and 10 percent GAN weight, respectively, for row 1: one model iteration and row 2: two model iterations (five-fold undersampling).

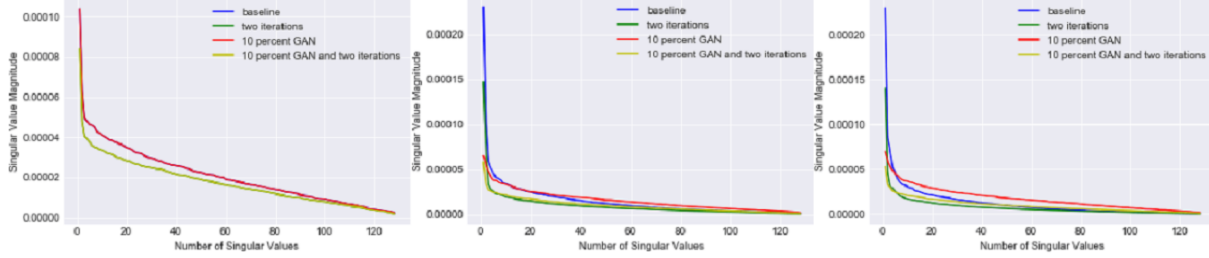


Figure 9. Singular value magnitudes after 1, 15K, and 30K iterations of training, respectively, for pure MSE loss and 10 percent GAN weight for both one and two model iterations (five-fold undersampling).

5. Discussions and conclusions

This paper introduces a series of experimental methods to better analyze uncertainty and understand the risks of hallucinated artifacts in compressive image recovery. To thoroughly explore the intersection of realistic and data consistent images, we develop a probabilistic VAE-GAN model, capable of reconstructing and generating medical images with high performance. We demonstrate the use of statistical methods in evaluating the models output distribution in addition to examining the Jacobians of the outputs with respect to the undersampled input data and their corresponding singular values. With both of these methods, we show the utility they can have in terms of gauging uncertainty and serving as a metric of comparison between different models or various hyperparameter settings.

In addition, we find that the risk of hallucination is greatly dependent on model parameters such as GAN loss, number of iterations, and undersampling rate, though moderate choices of such variables are seen to be fairly safe. Training

loss as well as the variance, bias, and error of the output reconstructions is higher as GAN loss increases, undersampling rate increases, and number of model iterations decreases. Furthermore, by examining the gradients of the output with respect to the aliased input images themselves, we see patterns in the singular values that suggest higher GAN loss and fewer model iterations make the VAE-GAN model more susceptible to adversarial perturbations in the inputs.

Due to the influence of these parameters, ongoing work is focused on understanding the specific effects of different data acquisition strategies on model robustness along with the development of regularization schemes capable of limiting hallucinations promoted by DL models in the high-frequency regime. Future work could involve exploring the effects of network capacity and quantity of training data on model uncertainty.

References

- URL <https://github.com/MortezaMardani/GAN-Hallucination/tree/vae>.
- [online] <http://mridata.org/fullysampled/knees.html>. URL <http://mridata.org/>.
- Bora, A., Jalal, A., Price, E., and Dimakis, A. G. Compressed sensing using generative models. *arXiv preprint arXiv:1703.03208*, 2017.
- Cheng, J. Y., Zhang, T., Alley, M. T., Lustig, M., Vasanawala, S. S., and Pauly, J. M. Variable-density radial view-ordering and sampling for time-optimized 3d cartesian imaging. In *Proceedings of the ISMRM Workshop on Data Sampling and Image Reconstruction*, 2013.
- Dieng, A. B., Kim, Y., Rush, A. M., and Blei, D. M. Avoiding latent variable collapse with generative skip models. *arXiv preprint arXiv:1807.04863*, 2018.
- Dosovitskiy, A. and Brox, T. Generating images with perceptual similarity metrics based on deep networks. In *Advances in Neural Information Processing Systems*, pp. 658–666, 2016.
- Greenspan, H., Van Ginneken, B., and Summers, R. M. Guest editorial deep learning in medical imaging: Overview and future promise of an exciting new technique. *IEEE Transactions on Medical Imaging*, 35(5): 1153–1159, 2016.
- Harrell, F. E., Lee, K. L., and Mark, D. B. Multivariable prognostic models: issues in developing models, evaluating assumptions and adequacy, and measuring and reducing errors. *Statistics in medicine*, 15(4):361–387, 1996.
- Henaff, M., Bruna, J., and LeCun, Y. Deep convolutional networks on graph-structured data. *arXiv preprint arXiv:1506.05163*, 2015.
- Hynynen, K., Darkazanli, A., Unger, E., and Schenck, J. MRI-guided noninvasive ultrasound surgery. *Medical Physics*, 20(1):107–115, 1993.
- Jégou, S., Drozdzal, M., Vazquez, D., Romero, A., and Bengio, Y. The one hundred layers tiramisu: Fully convolutional densenets for semantic segmentation. In *Computer Vision and Pattern Recognition Workshops (CVPRW), 2017 IEEE Conference on*, pp. 1175–1183. IEEE, 2017.
- Kendall, A. and Gal, Y. What uncertainties do we need in bayesian deep learning for computer vision? In *Advances in neural information processing systems*, pp. 5574–5584, 2017.
- Kingma, D. P. and Welling, M. Auto-encoding variational Bayes. *arXiv preprint arXiv:1312.6114*, 2013.
- Lee, D., Yoo, J., and Ye, J. C. Deep residual learning for compressed sensing mri. In *Biomedical Imaging (ISBI 2017), 2017 IEEE 14th International Symposium on*, pp. 15–18. IEEE, 2017.
- Lustig, M., Donoho, D., and Pauly, J. M. Sparse mri: The application of compressed sensing for rapid mr imaging. *Magnetic Resonance in Medicine: An Official Journal of the International Society for Magnetic Resonance in Medicine*, 58(6):1182–1195, 2007.
- Mardani, M., Gong, E., Cheng, J. Y., Vasanawala, S. S., Zaharchuk, G., Xing, L., and Pauly, J. M. Deep generative adversarial neural networks for compressive sensing (GANCS) MRI. *IEEE Transactions on Medical Imaging*, 2018.
- Moosavi-Dezfooli, S.-M., Fawzi, A., Fawzi, O., and Frossard, P. Universal adversarial perturbations. In *2017 IEEE Conference on Computer Vision and Pattern Recognition (CVPR)*, pp. 86–94. Ieee, 2017.
- Mousavi, A., Patel, A. B., and Baraniuk, R. G. A deep learning approach to structured signal recovery. In *Communication, Control, and Computing (Allerton), 2015 53rd Annual Allerton Conference on*, pp. 1336–1343. IEEE, 2015.
- Papernot, N., McDaniel, P., Jha, S., Fredrikson, M., Celik, Z. B., and Swami, A. The limitations of deep learning in adversarial settings. In *Security and Privacy (EuroS&P), 2016 IEEE European Symposium on*, pp. 372–387. IEEE, 2016.
- Pezeshki, M., Fan, L., Brakel, P., Courville, A., and Bengio, Y. Deconstructing the ladder network architecture. In *International Conference on Machine Learning*, pp. 2368–2376, 2016.
- Quan, T. M., Nguyen-Duc, T., and Jeong, W.-K. Compressed sensing MRI reconstruction with cyclic loss in generative adversarial networks. *arXiv preprint arXiv:1709.00753*, 2017.
- Radford, A., Metz, L., and Chintala, S. Unsupervised representation learning with deep convolutional generative adversarial networks. *arXiv preprint arXiv:1511.06434*, 2015.
- Tibshirani, R. *Bias, variance and prediction error for classification rules*. Citeseer, 1996.
- Tygart, M., Ward, R., and Zbontar, J. Compressed sensing with a jackknife and a bootstrap. *arXiv preprint arXiv:1809.06959*, 2018.

van den Oord, A., Vinyals, O., et al. Neural discrete representation learning. In *Advances in Neural Information Processing Systems*, pp. 6306–6315, 2017.

Vasanawala, S. S. and Lustig, M. Advances in pediatric body mri. *Pediatric radiology*, 41(2):549, 2011.

Xu, L., Ren, J. S., Liu, C., and Jia, J. Deep convolutional neural network for image deconvolution. In *Advances in Neural Information Processing Systems*, pp. 1790–1798, 2014.

Yang, G., Yu, S., Dong, H., Slabaugh, G., Dragotti, P. L., Ye, X., Liu, F., Arridge, S., Keegan, J., Guo, Y., et al. Dagan: Deep de-aliasing generative adversarial networks for fast compressed sensing MRI reconstruction. *IEEE Transactions on Medical Imaging*, 37(6):1310–1321, 2018.

Zhu, B., Liu, J. Z., Cauley, S. F., Rosen, B. R., and Rosen, M. S. Image reconstruction by domain-transform manifold learning. *Nature*, 555(7697):487, 2018.